Rodent Model of Brain Radionecrosis using Clinical LINAC-based Stereotactic Radiosurgery

Sean P. Devan M.S. , Guozhen Luo M.S. , Xiaoyu Jiang Ph.D. , Jingping Xie Ph.D. , Daniel Dean D.M.P. , Levi S. Johnson D.M.P. , Manuel Morales-Paliza Ph.D. , Hannah Harmsen M.D. , Junzhong Xu Ph.D. , Austin N. Kirschner M.D., Ph.D.

PII: S2452-1094(22)00120-8
DOI: https://doi.org/10.1016/j.adro.2022.101014
Reference: ADRO 101014

To appear in: *Advances in Radiation Oncology*

Received date: 21 December 2021
Accepted date: 21 June 2022

Please cite this article as: Sean P. Devan M.S. , Guozhen Luo M.S. , Xiaoyu Jiang Ph.D. , Jingping Xie Ph.D. , Daniel Dean D.M.P. , Levi S. Johnson D.M.P. , Manuel Morales-Paliza Ph.D. , Hannah Harmsen M.D. , Junzhong Xu Ph.D. , Austin N. Kirschner M.D., Ph.D. , Rodent Model of Brain Radionecrosis using Clinical LINAC-based Stereotactic Radiosurgery, *Advances in Radiation Oncology* (2022), doi: https://doi.org/10.1016/j.adro.2022.101014

Rodent Model of Brain Radionecrosis using Clinical LINAC-based Stereotactic Radiosurgery

Sean P. Devan, M.S.[1,2], Guozhen Luo, M.S.[3], Xiaoyu Jiang, Ph.D.[2,5], Jingping Xie, Ph.D.[2], Daniel Dean, D.M.P.[3], Levi S. Johnson, D.M.P.[3], Manuel Morales-Paliza, Ph.D.[3], Hannah Harmsen, M.D.[4], Junzhong Xu, Ph.D.[2,5], Austin N. Kirschner, M.D., Ph.D.[3]**

Affiliations:
1. Chemical and Physical Biology Program, Vanderbilt University, Nashville, TN, 37232 USA
2. Vanderbilt University Institute of Imaging Science, Vanderbilt University Medical Center, Nashville, TN, 37232 USA
3. Department of Radiation Oncology, Vanderbilt University Medical Center, Nashville, TN, 37232 USA
4. Department of Pathology, Microbiology and Immunology, Vanderbilt University Medical Center, Nashville, TN, 37232 USA
5. Department of Radiology and Radiological Sciences, Vanderbilt University Medical Center, Nashville, TN, 37232 USA

**Corresponding author: Austin N. Kirschner, Department of Radiation Oncology, Vanderbilt University Medical Center, 2220 Pierce Ave, B-1003 PRB, Nashville, TN, 37232, USA email: austin.kirschner@vumc.org, Telephone: 615-322-2555.

Word Count (excluding title page, abstract, figures/tables legends, references): 3393 words
Abstract Count: 232 words
References: 38
Total Figures and Tables: 5 Figures, 1 Table, 2 Supplementary Figures

Running Title: Rodent Model Brain Radionecrosis

Keywords. Stereotactic Radiosurgery, radionecrosis, MRI, brain, rodent model

Financial Disclosure/Conflicts of Interest. The authors have no financial disclosure or conflicts of interest related to this manuscript.

Funding. This study was supported by NIH grants K12CA090625, R01CA109106, and the Vanderbilt Radiology/VUIIS Catalyst Award Program. The imaging was supported by grant S10OD019993 for the Advance III HD Console of a 7T Small Animal MRI/MRS System housed in the Vanderbilt Center for Small Animal Imaging. The Translational Pathology Shared Resource is supported by NCI/NIH Cancer Center Support Grant P30CA068485 and the Vanderbilt Mouse Metabolic Phenotyping Center Grant U24DK059637.

Authors' Contributions:
Conception and Design: J. Xu, A.N. Kirschner
Development of Methodology: S.P. Devan, G. Luo, X. Jiang, J. Xie, D. Dean, L. Johnson, M. Morales-Paliza, J. Xu, A.N. Kirschner
Acquisition of Data: S.P. Devan, G. Luo, X. Jiang, J. Xie, H. Harmsen
Analysis and interpretation of data: S.P. Devan, G. Luo, X. Jiang, J. Xie, H. Harmsen, J. Xu, A.N. Kirschner
Writing, review, and/or revision of the manuscript: S.P. Devan, G. Luo, J. Xu, A.N. Kirschner
Administrative, technical, or material support: S.P. Devan, G. Luo, X. Jiang, J. Xie, D. Dean, L. Johnson, M. Morales-Paliza, H. Harmsen, J. Xu, A.N. Kirschner
Study supervision: J. Xu, A.N. Kirschner

Declaration of interests

The authors declare that they have no known competing financial interests or personal relationships that could have appeared to influence the work reported in this paper.

ABSTRACT

Purpose

To develop a rodent model of brain radionecrosis using clinical linear accelerator (LINAC)-based stereotactic radiosurgery (SRS).

Methods

Single fraction maximum prescription points in the mouse left hemisphere were irradiated using LINAC-based SRS with multiple arcs at 60 (N=5), 100 (N=5), and 140 (N=5) Gy. Rats (N=6) were similarly treated with 140 Gy. Gadolinium (Gd)-enhanced MRI was used to track radiation injury in mice over weeks (100 and 140 Gy) or months (60 Gy). Target accuracy was measured by the distance from the prescription point to the center of the earliest Gd-MRI enhancement. Confirmation of necrosis via histology was performed at the subject endpoints.

Results

Radiation injury as indicated by Gd-MRI was first identified at 2 weeks (140 Gy), 4-6 weeks (100 Gy), and 8 months (60 Gy). A volumetric time course shows rapid growth in the volume of Gd-MRI signal enhancement following the appearance of apparent necrosis. Histopathological features were consistent with radionecrosis.

Conclusions

The presented method uses a commonly available clinical linear accelerator to induce radiation necrosis in both mice and rats. The treatment is modeled after patient therapy for a more direct model of human tissue under a range of doses used in clinical neuro-ablation techniques. The short time to onset of apparent necrosis, accurate targeting of the prescription point, high incidence of necrosis, and similar pathologic features make this a suitable animal model for further research in radionecrosis.

INTRODUCTION

Neurologic injury is generally a late side effect of radiation therapy, occurring months after the treatment has occurred. Histological findings include inflammatory changes such as reactive gliosis, demyelination, white matter necrosis, and vascular changes in both the white matter tracts and central gray matter (1). Apoptosis of vascular endothelial cells may compromise the barrier between the circulatory system and neurologic tissue, as well as reduce the density of oligodendrocyte progenitor cells (1ï 3). It is thought that both mechanisms contribute to radiation injury of neurologic tissue (3).

Radiation treatment for some neurologic diseases utilizes the purposeful injury of nerve or brain tissues. Examples of modern radiotherapy include the treatment of medically-refractory trigeminal neuralgia (4), essential tremor and Parkinsonian tremor (5ï 8), epilepsy (9), and obsessive-compulsive disorder (10). Typically, these are treated with high-dose short-course radiotherapy delivered in a focused and precisely designed treatment technique known as stereotactic radiosurgery (SRS).

More commonly, radiotherapy is used to treat malignancies of the central nervous system, both primary tumors of neurologic tissues as well as metastatic disease, which treatments are supported by numerous clinical trials (11ï 13). However, there is a highly problematic clinical dilemma of differentiating tumor recurrence versus radiation necrosis (14). This confounding situation often leads to delay in management of the true ongoing pathology, which can have significant detriment to patient care (15). Clinical factors have been associated with rates of radionecrosis, such as the volume of normal brain tissue receiving dose levels, e.g., 21 Gy for single-fraction SRS (16), maximum tumor diameter (17), and single-fraction versus multi-fraction SRS (18). Unfortunately, radionecrosis is indistinguishable from tumor recurrence on clinical standard-of-care MRI with gadolinium (Gd)-based contrast agents due to the breakdown of blood brain barrier (BBB) in both types of lesions. Furthermore, besides dose constraints, what factors may help reduce the risk of radionecrosis are unknown.

It is impossible to study the effects of radionecrosis on neurologic tissues directly in healthy human brains and hence animal models of radionecrosis are necessary. It is therefore of interest to develop an animal model of brain radionecrosis in both rats and mice that allows high maximum doses with minimal toxicity to the animals. LINAC-based SRS with multiple arcs is becoming more widespread and growing in availability, which allows efficient treatment of both small and large neurologic tumors with minimized dose spillover to surrounding normal-appearing brain tissues (19). Recently, clinical studies have used LINAC-based SRS to treat essential tremor patients (8, 20). These studies use single fraction, highly-focused (~4 mm), and high dose (maximum 162 Gy) plans to irradiate the ventral intermediate nucleus (VIM) of the thalamus and induce radionecrosis. A recent study has shown the dosage deliveray can be accurate with an overall three-dimensional uncertainty of 1.1 mm in patients and sub-mm in each dimension (21). This approach makes it possible to generate radionecrosis in small animal brains with high accuracy and high dosage. However, LINAC SRS in clinics typically uses cone sizes Ó 4 mm, which is comparable to the size of the mouse brain hemisphere. It is so far unknown if the dose volumes of this clinical approach could cause similarly severe toxicity as in whole brain or whole hemisphere treatments in small animals. This could impact the development of radionecrosis and may shorten animal lifespans, both of which are not desirable. In this work, we translate such a clinically available LINAC-based SRS protocol to both rats and mice to demonstrate the feasibility of this brain radionecrosis model.

MATERIALS AND METHODS

Ethics statement

All animal-related studies were approved by local IACUC. The imaging and irradiation experiments were performed with anesthesia and minimum suffering to the animals.

Radiation treatment planning

Treatment plans were developed mimicking high-dose SRS patient treatment plans, including the use of up to 10 rotational arcs focused on a single isocenter. The iPlan® system (Version 4.5.5; Brainlab company; Munich, Germany) was the treatment planning system to design all the plans for the mice. A high-resolution CT (voxel size of $0.2\times0.2\times0.2mm^3$) of a same-age mouse was imported into iPlan® RT dose for treatment planning. Our smallest stereotactic radiosurgery SRS cone of 4 mm from Brainlab was selected to minimize dose to surrounding brain tissue. The isocenter was placed at one-third to the left side in the left to right (LR) direction, midline in the anterior to posterior (AP; i.e. rostral-caudal) direction, and midline in the superior to inferior (SI; i.e. dorsal-ventral) direction. For this study, we used three different prescription levels of 140 Gy, 100 Gy, and 60 Gy with five mice each. The maximum dose of 140 Gy was chosen to replicate the range of SRS treatments for tremor patients (8, 20, 21). One cohort of six rats was treated with 140 Gy using a similar plan to test feasibility across species. To further spare the normal tissue from the radiation damage, arc therapy instead of static fields was chosen to deliver the dose. The geometry of every plan, including the couch and gantry angles, remain the same for different dose levels, and the numbers of monitor units (MUs) were renormalized to deliver the prescription dose to isocenter. A total of ten arcs with the same dose weight of each arc to isocenter were utilized. Table 1 shows the gantry and couch angles of the plans both in the Varian convention and the matching IEC convention.

Radiation plan delivery

The animals used were age-matched female CD-1 mice (Envigo; Indianapolis, IN, USA) and male Fischer rats (F344/NHsd; Envigo; Indianapolis, IN, USA). Mice were treated at 6 weeks of age around 20 g, and rats at 6-7 weeks around 210 g. Mouse and rat radiation was administered with a clinical Novalis TX^{TM} (Varian Medical Systems, Inc; Palo Alto, California). All the animals were planned and treated in head-first prone position. During treatment, each animal was under anesthesia with 2%/98% isoflurane/O_2 and was placed in a 3D printed animal holder to minimize motion. On-board imaging by cone-beam CT (CBCT) was used to target the brain isocenter. CBCT was performed with the high-quality head protocol with a full bow tie. A reconstruction size of 5 × 5 cm, thickness of 2 mm, and matrix size of 512×512 pixels were used. After the CBCT, coregistration with the planning CT was performed on the console and the couch was moved to plan isocenter by automated robotics. Figure 2 shows the axial, coronal, and sagittal views with isocenter and brain contour overlays. After the couch was moved to the plan isocenter, all ten planned arcs were delivered. The total radiation delivery time including onboard imaging was less than ~30 minutes for the highest dose cohort. Less delivery time is needed for smaller dose levels due to the use of fewer MUs.

Monitoring and confirmation of lesion progression

Radionecrotic lesions were identified in mice by Gd-enhanced T1- and T2-weighted 2D fast spin echo MRI with an image size 128x128 and a slice thickness of 500 µm using a Bruker (Bruker Corporation; Billerica, Massachusetts) 7.0 Tesla, 16 cm bore horizontal scanner. All animals were anesthetized using 1-2%/98% isoflurane/O_2. A dose of 2.5 mmol/kg of Gd contrast (gadobutrol, Gadavist; Bayer HealthCare Pharmaceuticals Inc; Whippany, New Jersey) was administered intraperitoneally (IP) 10 minutes prior to imaging in mice and 0.6 mmol/kg via

jugular catheter injection in rats 15-20 minutes prior to imaging. One rat had an unexpected delay after injection so it was excluded from the volume analysis. Mice with 100 and 140 Gy treatments were imaged over the span of 90 days from treatment. Mice with 60 Gy were imaged at 1, 2, 4, and 8 months. Rats with 140 Gy were imaged at a single time point at 8 weeks. At the final time point, animals were sacrificed via transcardial perfusion of 10% formalin, and brain tissues were fixed by immersion in formalin for two days, and then stored in 70% ethanol. Hematoxylin and eosin (H&E) staining with a slice thickness of 8 μm was used in the histology analysis for confirmation of radiation necrosis.

RESULTS

Dosimetry

The relative isodose distribution lines and arc arrangement in mice are shown in Figure 1**.** This figure shows that the multiple arc technique can significantly reduce the dose to surrounding tissues. In mice, the 50% isodose line has slight spillage into the contralateral brain, with 1% hemispheric volume above this dose. In rats, the maximum dose in the contralateral brain was 32% (45 Gy for our 140 Gy cohort). Supplemental figures S1 and S2 include relative dose-volume histograms in the ipsilateral and contralateral hemispheres for both mice and rats, respectively.

Imaging lesion volume and accuracy

All irradiated rats and mice developed apparent necrosis before sacrifice, except for one 60 Gy subject who did not survive until the 8-month time point. All mice treated with 140 Gy first showed Gd-T1w MRI hyperintensity at 2 weeks following treatment. Two of the 100 Gy mice showed enhancement at 4 weeks and all showed enhancement by 6 weeks. The 60 Gy mice first showed enhancement at 8 months. Rats receiving 140 Gy showed radionecrosis at 8 weeks.

Lesion volumes for the three groups of mice are shown in Figure 3. Volume was measured by hand-drawing ROIs containing regions that were hyperintense on Gd-T1w MRI in the treated hemisphere relative to the contralateral side. Figure 3 shows a representative slice in a 140 Gy mouse at week 2 with the corresponding ROI. At the initial time point (2 weeks) the 140 Gy mice had a volume of 26.5 ± 1.0 mm^3 (mean ± SD) and grew to 97.6 ± 26.8 mm^3. The two 100 Gy subjects showing necrosis at 4 weeks had volumes of 7 and 10 mm^3. These subjects showed much larger volumes (both 29 mm^3) at week 6 than those first presenting at that timepoint (11-16 mm^3) and continued to show larger lesion growth (1.9 mm^3/day versus 0.6 mm^3/day). The 100 Gy cohort had an enhancement volume of 77 mm^3. This is compared to a volume of 49 mm^3 in a previous study using Gamma Knife (22); this discrepancy may be due to the different isocenter location in the two models, with the Gamma Knife lesion being more superficial, or a difference in volume estimation methods. Five rats showed enhancement volume of 143 ± 20 mm^3 at 8 weeks, which is substantially larger than the mice at the same dose and time point (69 ± 29 mm^3).

Targeting accuracy was determined by first calculating the geometric centroid (i.e., the average position of all voxels) of the lesion ROI as a surrogate for the delivery isocenter. The 140 Gy mice showed the tightest volume distribution and earliest time point with a visible lesion on Gd-MRI, so the images of this group at the 2 week time point were chosen to most accurately represent the beam location. Because the only difference in treatment between the different groups of mice was the number of MUs delivered, which should not affect geometry, the accuracy of the 140 Gy group is sufficient to characterize all groups. The prescription point was then estimated as the point 50% SI, 50% AP, and 33% LR of the brain on the MR images. The

Euclidean distance between the prescription point and the center of the lesion defined the delivery accuracy. Figure 4A-B shows a representative subject with the two points overlaid. Figure 4C summarizes the result for all subjects. The mean distance of the five subjects was 1.0 ± 0.2 mm, which is comparable to the targeting accuracy of 1.1 mm in patients (21). The largest variance was in the SI direction (mean distance 0.7 mm), possibly due to motion from the subject breathing.

Histological confirmation of necrosis

Digital H&E cross-sections of excised brains were viewed by a pathologist using QuPath-0.3.0 (23). All sections demonstrated evidence of radiation injury as shown in Figure 5, including vascular telangiectasia, vessel wall hyalinization, fibrinoid necrosis of blood vessels, intravascular thrombosis, edema, neuron and parenchyma loss, gliosis, microcavitation, cavitation, infiltrates of foamy macrophages, and neutrophil infiltration. Microhemorrhages were encountered in nearly all cases, and a larger hemispheric hemorrhage was present in one case. Most histologic changes were confined to the hemisphere ipsilateral to the radiation; however, two cases showed changes in the contralateral hemisphere. The case with a large hemorrhage had extension of the hemorrhage across the corpus callosum into the contralateral hemisphere, and one case had dilated vessels extending into the contralateral thalamus.

While the above features indicative of radiation effect were seen, there were differences between the various groups. While nearly all cases reviewed had vascular dilatations (telangiectasias), vessel wall hyalinosis and/or fibrinoid necrosis, microhemorrhages, and microcavitation with neuron loss, these features were relatively more prominent in the 100 Gy mice in comparison to the other groups (140 Gy mice and rats). Conversely, regions of cavitation, tissue necrosis, macrophage infiltrates, neutrophil infiltrates, and gliosis were more frequent in the 140 Gy mouse and rat groups.

Toxicity effects from treatment

Some of the mice treated with 140 and 100 Gy showed alopecia on the region of the scalp near the isocenter. None of the 60 Gy mice or 140 Gy rats showed any alopecia. No moist desquamation, esophagitis, oral cavity irritation, or change in animal behavior was observed in any group. One 140 Gy mouse showed herniation of the brain midline at 5 weeks and was sacrificed. This mouse was included in volume measurements prior to but not including the observed herniation. One 60 Gy mouse was sacrificed without imaging prior to the 8-month timepoint due to severe hemorrhage.

DISCUSSION

This study demonstrates the feasibility of a multi-arc LINAC-SRS-based small animal model of radiotherapy in rats and mice. To the best of our knowledge, this is the first study to generate radionecrosis in mouse brains using a clinical LINAC. Treatment planning on CT simulation as well as registration and alignment with high-resolution onboard CBCT allowed for accurate targeting in small animal brains comparable to that in patients. Successful delivery using a wide range of doses (60-140 Gy) demonstrates the flexibility of this method to accommodate even the ultra-high doses used in patients to date. The high incidence of radionecrosis in multiple species indicates this method can be applied to both rat and mouse tumor and/or necrosis models. The lesion volumes were tracked over time in the 100 and 140 Gy mice and showed growth over 13 weeks following treatment. The steady initial growth, high incidence, short time to onset, and low variance of lesion volume at the initial time point in the 140 Gy cohort are desirable characteristics of an animal model of radiation necrosis. The histopathological features of the tissues at their endpoints are consistent with radionecrosis. The dose-

dependence of these features highlights a potential qualitative difference in injury induced by higher dose neuro-ablation techniques versus lower dose in cancer therapies, and motivates future study of this relationship.

Preclinical models in animals to evaluate novel radiotherapies, radioprotective pharmaceuticals, and imaging methods are an essential step toward human implementation in clinical radiation oncology. Typically, radionecrosis is generated in one hemisphere of the animal and the contralateral hemisphere serves as a control. It is a challenging procedure due to the small size of rodent brains. To this end, specialized small animal irradiators have been developed and successfully implemented to induce radionecrosis in mice (24, 25), but such a model requires dedicated preclinical equipment that is not broadly available. Clinical equipment such as Gamma Knife has been used in rats (26, 27) and mice (22, 28, 29). These models use the high precision of Gamma Knife SRS to induce radionecrosis in small animal brains and have been extensively characterized using imaging and histology. However, Gamma Knife is not widely available to clinics, which limits how translatable it is to many institutions. To overcome this disadvantage, the linear accelerator (LINAC), which is more commonly used in clinics, has been applied in rats (30, 31). This model uses a single beam delivery but suffers toxicity such as moist desquamation dermatitis from a 60 Gy treatment (20). This may limit the maximum deliverable dose using a single beam, which is undesirable to study radionecrosis induced by higher doses such as 140 Gy used in the SRS treatments of tremor patients (8, 20). Moreover, rats are relatively more expensive and less used than mouse models particularly in cancer research. This may limit the ability to study large cohorts to investigate several hypotheses and make strong statistical conclusions.

Although animal models of radiation treatment have existed for decades, keeping these models relevant to the rapidly emerging technologies in human care is nontrivial. For instance, clinical SRS has shown to have benefits over whole-brain radiotherapy (WBRT) in treating brain metastases (32), but requires accurate targeting that may be difficult to implement in mice (33). Dedicated preclinical irradiators have grown in sophistication to meet such challenges. Small animal irradiators with onboard imaging allow for highly accurate target localization and radiation delivery (34). However, these machines generally do not fully replicate human therapies, for example, differing in dose rate and beam quality (35). Furthermore, mice are sensitive to long durations of anesthesia (33), so the low dose rate of small animal irradiators may endanger the animals in the case of high-dose therapies. The use of clinical machines may therefore have advantages in cases where sub-millimeter targeting can be sacrificed for a more exact model of radiation. For this reason, several models of radiation necrosis in small animals have used clinical machines for irradiation. Gamma Knife has successfully delivered high doses (60 Gy prescribed at the 50% isodose line) to small volumes in mice (22), but clinical Gamma Knife generally suffers from a lower dose rate than LINAC-based methods (36) and may prolong an animalôs time under anesthesia. Our treatment model in this study used a clinical machine to normalize effects of beam quality and treatment time on pathological response to radiation. The high dose rate of clinical LINAC facilitates high subject throughput and mitigates negative effects from prolonged time under anesthesia. In fact, modern LINACs that have flattening filter free (FFF) mode can deliver dose at least twice as fast as the LINAC used in our study.

Relative to other models of radiation necrosis using clinical LINAC, hypofractionated SRS enables higher doses in smaller volumes than previously published in mice. The plans used in this study were modeled after the highest doses used in patients with small treatment volumes. Our mice showed only mild observable toxicity in our maximum 140 Gy dose with multiple circular photon arcs. Such a high dose would not be achievable without severe toxicity using a single field beam. Because biopsy is not clinically accessible in many such CNS therapies, an

animal model able to accommodate these doses allows further study of the effect of high dose radiation on tissues *in vivo*. Furthermore, an *in vivo* model accurately replicating human therapies which can be monitored over time by imaging histology or imaging allows for better testing of drugs and novel imaging methods.

The results of this study preliminarily demonstrate the feasibility of generating radionecrosis in both mice and rats using LINAC-SRS. BBB breakdown as indicated by Gd-MRI was used as a biomarker for necrosis, but a histology time-course could further elucidate what pathological changes occur other than detected by perfusion. The histological results in this study demonstrate that fibrinoid necrosis does occur, but a larger study could enable quantitative grading of the extent of necrosis for comparisons between doses. BBB breakdown was also used as a marker to localize dose delivery and measure treatment accuracy. An alternative assessment of accuracy performed by Kim et al. to characterize Cyber Knife targeting in mice was to sacrifice the subjects shortly after treatment and perform staining sensitive to DNA strand breaks (37). DNA damage is likely a more direct biomarker than BBB breakdown for localizing radiation, but is unobtainable *in vivo*. Because eliminating geometric distortions between the excised tissue and the *in vivo* volume is not trivial (38), Gd-MRI may nonetheless have advantages for localizing radiation.

CONCLUSIONS

We demonstrate the feasibility of a LINAC-based SRS treatment of mice and rats with single fraction doses comparable to the highest used in patients. BBB breakdown as indicated with Gd-MRI develops with a short time to onset, high spatial localization, and high incidence. Due to the widespread availability of SRS-capable LINAC machines, this is an accessible model for the investigation of radionecrosis pathology, drugs to mitigate patient toxicity, and novel imaging methods.

References

1. Wong CS, Fehlings MG, Sahgal A. Pathobiology of radiation myelopathy and strategies to mitigate injury. *Spinal Cord*. 2015;53:574ï 580.

2. Li Y-Q, Chen P, Haimovitz-Friedman A, *et al.* Endothelial Apoptosis Initiates Acute Bloodï Brain Barrier Disruption after Ionizing Radiation. *Cancer Res.* 2003;63:5950 LP ï 5956.

3. Coderre JA, Morris GM, Micca PL, *et al.* Late effects of radiation on the central nervous system: role of vascular endothelial damage and glial stem cell survival. *Radiat. Res.* 2006;166:495ï 503.

4. Tuleasca C, Régis J, Sahgal A, *et al.* Stereotactic radiosurgery for trigeminal neuralgia: a systematic review. *J. Neurosurg.* 2018;130:733ï 757.

5. Dallapiazza RF, Lee DJ, De Vloo P, *et al.* Outcomes from stereotactic surgery for essential tremor. *J. Neurol. Neurosurg. Psychiatry*. 2019;90:474ï 482.

6. Martínez-Moreno NE, Sahgal A, De Salles A, *et al.* Stereotactic radiosurgery for tremor: systematic review. *J. Neurosurg.* 2018;130:589ï 600.

7. Pérez-Sánchez JR, Martínez-Álvarez R, Martínez Moreno NE, *et al.* Gamma Knife® stereotactic radiosurgery as a treatment for essential and parkinsonian tremor: long-term experience. *Neurologia*. 2020.

8. Luo G, Cameron BD, Wang L, *et al.* Targeting for stereotactic radiosurgical thalamotomy based on tremor treatment response. *J. Neurosurg.* 2021:1ï 8.

9. Kondziolka D, Flickinger JC, Lunsford LD. Stereotactic radiosurgery for epilepsy and functional disorders. *Neurosurg. Clin. N. Am.* 2013;24:623ï 632.

10. Martínez-Álvarez R. Radiosurgery for Behavioral Disorders. *Prog. Neurol. Surg.* 2019;34:289ï 297.

11. Barani IJ, Larson DA. Radiation therapy of glioblastoma. *Cancer Treat. Res.* 2015;163:49ï 73.

12. Soliman H, Das S, Larson DA, *et al.* Stereotactic radiosurgery (SRS) in the modern management of patients with brain metastases. *Oncotarget*. 2016;7:12318ï 12330.

13. Thiagarajan A, Yamada Y. Radiobiology and radiotherapy of brain metastases. *Clin. Exp. Metastasis*. 2017;34:411ï 419.

14. Fink J, Born D, Chamberlain MC. Radiation necrosis: relevance with respect to treatment of primary and secondary brain tumors. *Curr. Neurol. Neurosci. Rep.* 2012;12:276ï 285.

15. Miyatake S, Nonoguchi N, Furuse M, *et al.* Pathophysiology, diagnosis, and treatment of radiation necrosis in the brain. *Neurol. Med. Chir. (Tokyo).* 2015;55:50ï 59.

16. Doré M, Martin S, Delpon G, *et al.* Stereotactic radiotherapy following surgery for brain metastasis: Predictive factors for local control and radionecrosis. *Cancer Radiother.* 2017;21:4ï 9.

17. Kohutek ZA, Yamada Y, Chan TA, *et al.* Long-term risk of radionecrosis and imaging changes after stereotactic radiosurgery for brain metastases. *J. Neurooncol.* 2015;125:149ï 156.

18. Minniti G, Scaringi C, Paolini S, *et al.* Single-Fraction Versus Multifraction (3 × 9 Gy)

Stereotactic Radiosurgery for Large (>2 cm) Brain Metastases: A Comparative Analysis of Local Control and Risk of Radiation-Induced Brain Necrosis. *Int. J. Radiat. Oncol. Biol. Phys.* 2016;95:1142ï 1148.

19. Park HS, Wang EH, Rutter CE, *et al.* Changing practice patterns of Gamma Knife versus linear accelerator-based stereotactic radiosurgery for brain metastases in the US. *J. Neurosurg.* 2016;124:1018ï 1024.

20. Khattab MH, Cmelak AJ, Sherry AD, *et al.* Noninvasive Thalamotomy for Refractory Tremor by Frameless Radiosurgery. *Int. J. Radiat. Oncol. Biol. Phys.* 2021.

21. Luo G, Neimat JS, Cmelak A, *et al.* Margin of error for a frameless image guided radiosurgery system: Direct confirmation based on posttreatment MRI scans. *Pract. Radiat. Oncol.* 2017;7:e223ï e231.

22. Jiang X, Yuan L, Engelbach JA, *et al.* A gamma-knife-enabled mouse model of cerebral single-hemisphere delayed radiation necrosis. *PLoS One*. 2015;10.

23. Bankhead P, Loughrey MB, Fernández JA, *et al.* QuPath: Open source software for digital pathology image analysis. *Sci. Reports 2017 71*. 2017;7:1ï 7.

24. Kiehl EL, Stojadinovic S, Malinowski KT, *et al.* Feasibility of small animal cranial irradiation with the microRT system. *Med. Phys.* 2008;35:4735.

25. Wong J, Armour E, Kazanzides P, *et al.* A high resolution small animal radiation research platform (SARRP) with x-ray tomographic guidance capabilities. *Int. J. Radiat. Oncol. Biol. Phys.* 2008;71:1591.

26. Kondziolka D, Lunsford LD, Claassen D, *et al.* Radiobiology of RadiosurgeryPart I. The Normal Rat Brain Model. *Neurosurgery*. 1992;31:271ï 279.

27. Mori Y, Kondziolka D, Balzer J, *et al.* Effects of Stereotactic Radiosurgery on an Animal Model of Hippocampal Epilepsy. *Neurosurgery*. 2000;46:157ï 168.

28. Jiang X, Engelbach JA, Yuan L, *et al.* Anti-VEGF antibodies mitigate the development of radiation necrosis in mouse brain. 2014;20:2695ï 2702.

29. Jiang X, Perez-Torres CJ, Thotala D, *et al.* A GSK-3þ inhibitor protects against radiation necrosis in mouse brain. *Int. J. Radiat. Oncol. Biol. Phys.* 2014;89:714ï 721.

30. Hartl BA, Ma HSW, Hansen KS, *et al.* The effect of radiation dose on the onset and progression of radiation-induced brain necrosis in the rat model. *Int. J. Radiat. Biol.* 2017;93:676ï 682.

31. Kumar S, Arbab AS, Jain R, *et al.* Development of a novel animal model to differentiate radiation necrosis from tumor recurrence. *J. Neuro-Oncology 2012 1083*. 2012;108:411ï 420.

32. Mainwaring W, Bowers J, Pham N, *et al.* Stereotactic Radiosurgery Versus Whole Brain Radiation Therapy: A Propensity Score Analysis and Predictors of Care for Patients With Brain Metastases From Breast Cancer. *Clin. Breast Cancer*. 2019;19:e343ï e351.

33. Yang L, Yang J, Li G, *et al.* Pathophysiological Responses in Rat and Mouse Models of Radiation-Induced Brain Injury. *Mol. Neurobiol. 2015 542*. 2016;54:1022ï 1032.

34. Sharma S, Narayanasamy G, Przybyla B, *et al.* Advanced Small Animal Conformal Radiation Therapy Device. *Technol. Cancer Res. Treat.* 2017;16:45ï 56.

35. Verhaegen F, Dubois L, Gianolini S, *et al.* ESTRO ACROP: Technology for precision small animal radiotherapy research: Optimal use and challenges. *Radiother. Oncol.* 2018;126:471ï 478.

36. Liu H, Andrews DW, Evans JJ, *et al.* Plan Quality and Treatment Efficiency for Radiosurgery to Multiple Brain Metastases: Non-Coplanar RapidArc vs. Gamma Knife. *Front. Oncol.* 2016;0:26.

37. Kim H, Fabien J, Zheng Y, *et al.* Establishing a process of irradiating small animal brain using a CyberKnife and a microCT scanner. *Med. Phys.* 2014;41:021715.

38. Sinha TK, Khatib-Shahidi S, Yankeelov TE, *et al.* Integrating spatially resolved three-dimensional MALDI IMS with in vivo magnetic resonance imaging. *Nat. Methods*. 2008;5:57.

FIGURE CAPTIONS

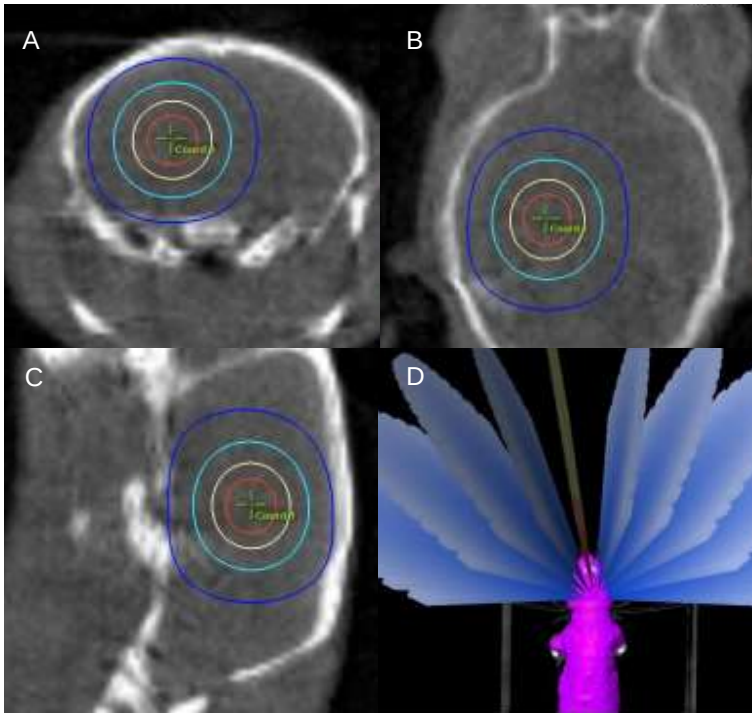

Figure 1. The isodose distribution lines for Axial (A), Coronal (B) and Sagittal (C) views for 90%, 75%, 50% and 25% dose level in a mouse brain. D shows the arc arrangement of the plan.

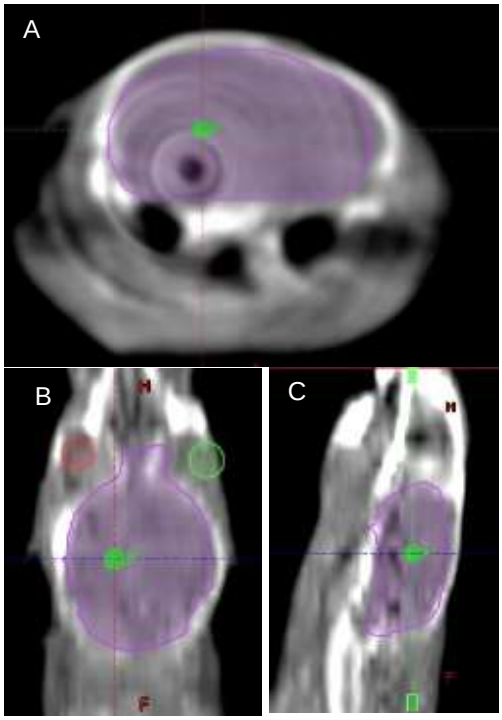

Figure 2. CBCT image in Axial (A), Coronal (B) and Sagittal (C) views with isocenter and brain contours

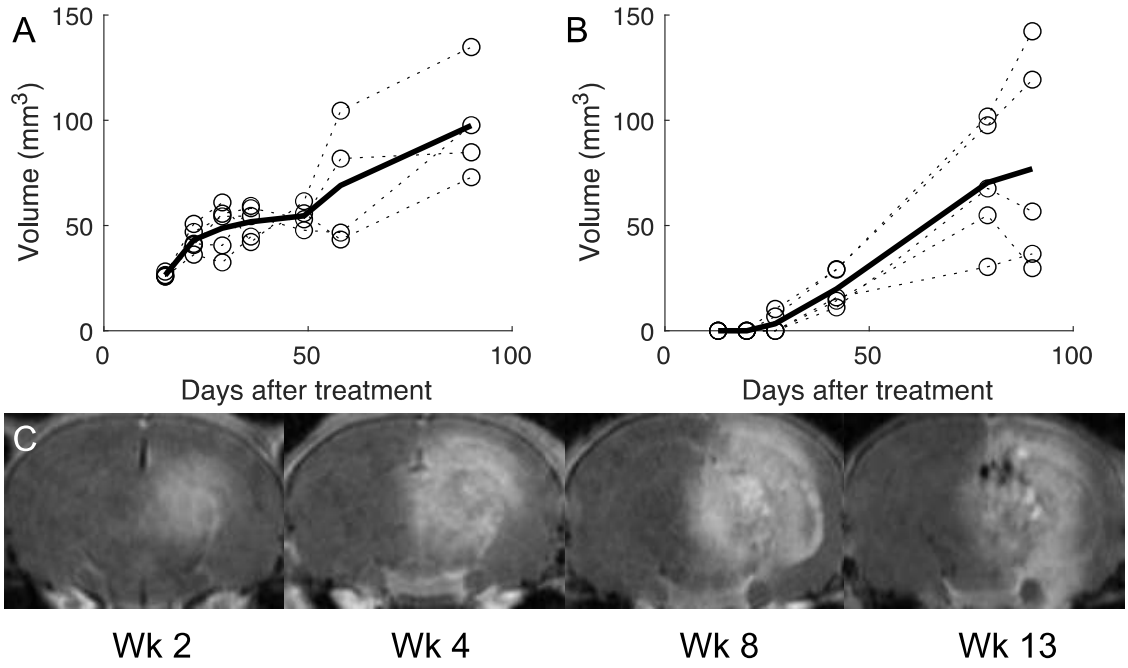

Figure 3. Volumetric assessment of radiation necrosis over time as assessed by Gd-MRI in 140 Gy (A) and 100 Gy (B) mice. Panel (C) shows a representative timecourse in Gd-T1w images in a 140 Gy mouse.

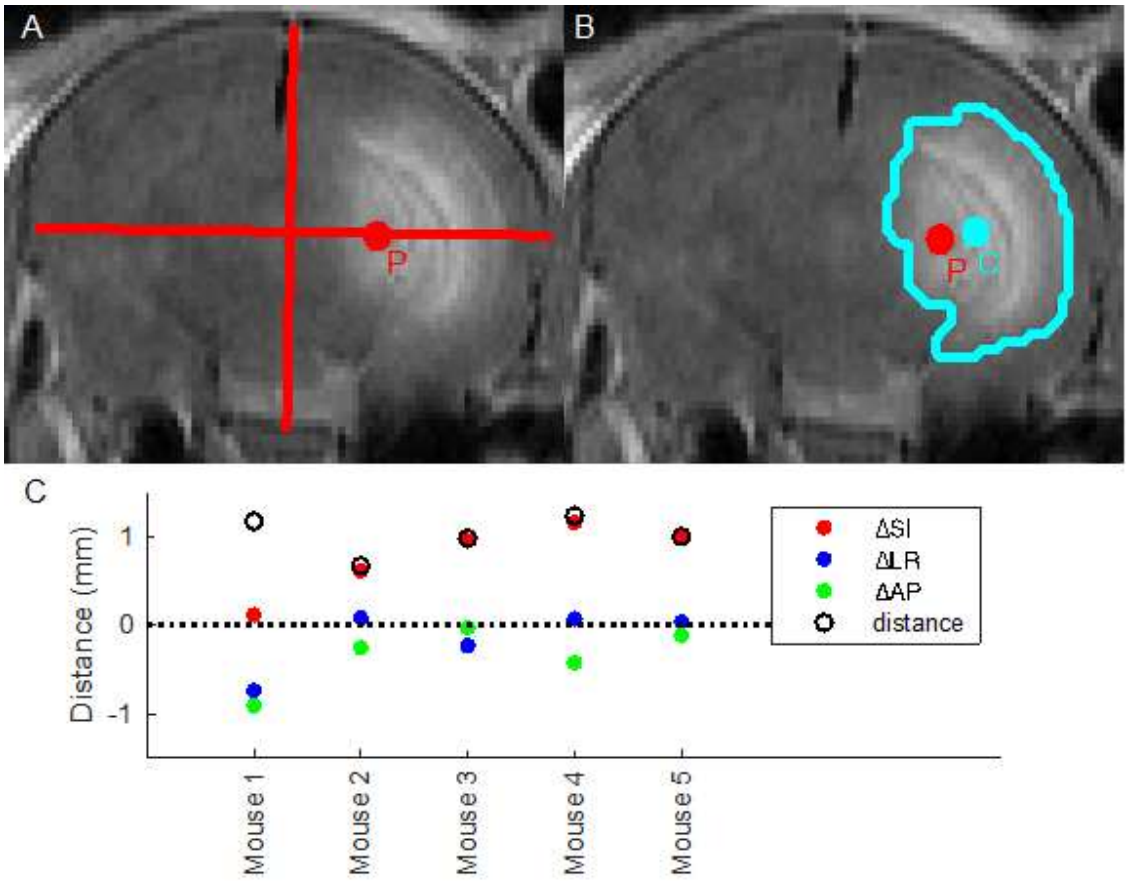

Figure 4. Calculation of accuracy by difference between anatomy and center of necrosis. (A) The prescription point P as was defined by 50% of the brain in the SI direction, 50% AP, and 33% LR. (B) ROIs were hand-drawn around the region of hyperintensity present in only one hemisphere. The geometric centroid C of the ROI (i.e., the mean coordinates of all ROI points) was used to estimate the isocenter. (C) Distance in all three dimensions of the prescription to the center of the ROI (i.e., P minus C). Total distance is the Euclidean norm of the points. The subject denoted ñMouse 1òis displayed in (A) and (B). Both panels show slice of point P.

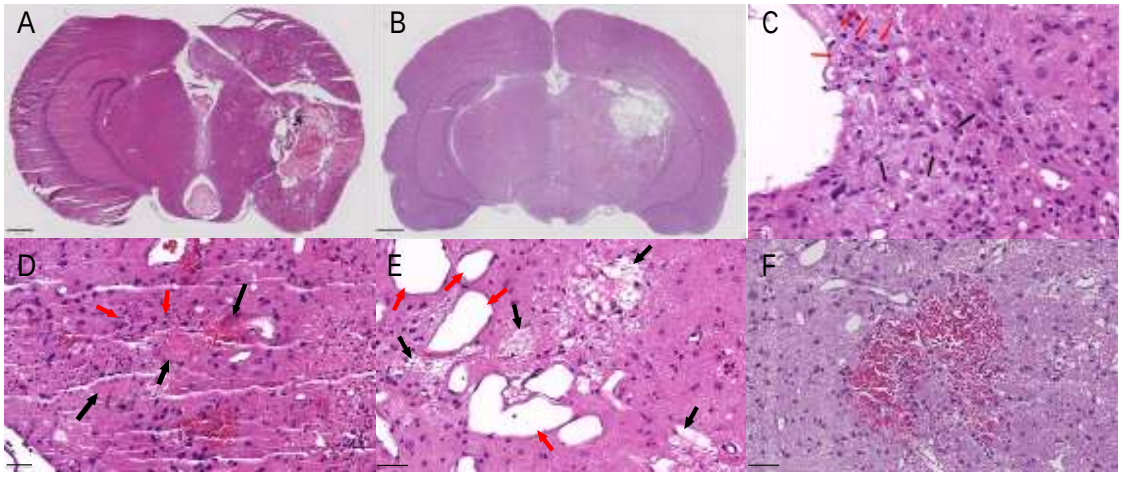

Figure 5. Example slides using H&E staining in 140 Gy mice (A) and rats (B). Features indicative of radionecrosis include reactive astrocytes (C black arrows), foamy macrophages (C red arrows), thrombosis (D red arrows), neutrophils (D black arrows), microcavitation (E black arrows), vascular dilation (E red arrows), microhemorrhage (F), and gliosis (F). Scale bars are 800 µm (A), 1,000 µm (B), 20 µm (C), and 50 µm (D-F).

TABLE CAPTIONS

		1	2	3	4	5	6	7	8	9	10
Couch angle (Varian convention)		260°	245°	230°	215°	200°	160°	145°	130°	115°	100°
Couch angle (IEC convention)		280°	295°	310°	325°	340°	20°	35°	50°	65°	80°
Gantry angle (Varian convention)	Start	150°	30°	150°	30°	150°	210°	330°	210°	330°	210°
	End	30°	150°	30°	150°	30°	330°	210°	330°	210°	330°
Gantry angle (IEC convention)	Start	30°	150°	30°	150°	30°	330°	210°	330°	210°	330°
	End	150°	30°	150°	30°	150°	210°	330°	210°	330°	210°

Table 1**.** Table and Gantry angles of the treatment plans in both Varian convention and IEC convention. All the treatments were administered with a system commissioned in Varian convention.